Multiphase Transport Modeling for Vacuum Drying of Pharmaceutical Products

Aditya G. Dodda and Michael A. Henson
Department of Chemical Engineering, University of Massachusetts, Amherst, MA 01003

Kostas Saranteas
Department of Chemical Engineering, Sunovion Pharmaceuticals Inc., Marlboro, MA

DOI 10.1002/aic.14879

Vacuum drying of active pharmaceutical ingredients (API) is an energy-intensive process that is often a manufacturing bottleneck. A multiphase transport model to predict drying performance under the assumption that boiling is the dominant mechanism is developed. Laboratory scale drying experiments were performed over a range of temperatures and pressures using acetone as the solvent and glass beads of three different particle sizes to mimic APIs. A two-phase transport model with the vapor and solid considered as one phase and the liquid treated as the second phase was capable of qualitatively reproducing the drying dynamics is found. Adjustable model parameters estimated from experimental data collected over a range of operating conditions exhibited trends that provided further insight into drying behavior. Boiling is the dominant mechanism in vacuum drying and our transport model captured the key physics of the process.

Keywords: vacuum drying, multiphase, transport model, mass spectrometer, glass beads

Introduction

Vacuum drying is a widely used unit operation in the pharmaceutical industry for reducing solvent levels of intermediate and final solid products to acceptable levels. Drying can be the rate limiting step in the cycle time of a pharmaceutical plant as it can require hours to days for completion.[1] The drying bottleneck motivates the quantitative investigation of the effect of drying process parameters on cycle times.

A promising approach for process improvement is to use a mathematical model to predict and optimize dryer performance. A wide variety of drying models exist[2] and can be conveniently classified as: (a) vaporization front models, (b) pore network models, (c) population balance models, (d) discrete element models, and (e) transport models. Vaporization front and population balance models typically contain numerous unknown parameters that must be estimated from dryer data.[2] Furthermore, the extensibility of these models to new operating condition as needed for process optimization has not been well studied. Pore network models are most useful for developing fundamental understanding of the impact of the cake pore structure on drying behavior. However, these models require substantial information about the cake structure and do not account for many important transport effects including nonisothermal operation. While they do not suffer from the limitations of the other drying models, discrete element models are highly computationally intensive as individual particles must be simulated.[2] Consequently, these models are not well suited for process simulation and optimization.

Whitaker developed a general theory of drying based on coupled heat and mass transfer.[3] A number of drying models with applications to pharmaceutical products[1,4] as well as in other industries[5,6] have been based on the Whitaker model. For example, variants of the Whitaker model have been developed for three-dimensional simulation of wood drying[7] and clay drying.[8] Because these models have the ability to generate qualitatively accurate predictions with reasonable computational effort, we also based the development of our vacuum drying model on the Whitaker model.

We observed from our experiments that the thermodynamics during vacuum drying were very similar to that of simple boiling. The same behavior was observed in another study on vacuum drying of pharmaceutical products with multiple solvents.[9] However, existing drying models including the Whitaker model do not account the thermodynamics of boiling. Therefore, the goal of this study was to develop a novel multiphase drying model that captured the boiling mechanism. To avoid the complexities of a full three-phase model, we considered the system to comprise of two phases: the liquid phase and a combined solid-vapor phase. As opposed to drying models in which the rate of liquid vaporization was calculated from empirical relationships, we used the liquid phase energy balance to rigorously compute the mass loss due to boiling. Cake temperature and solvent composition data collected over a range of temperatures, pressures, and glass bead sizes were used to identify parameter trends and obtain further insights into drying behavior. While we focused on vacuum tray drying, the proposed model can be extended to other vacuum drying processes such as agitated Nutsche dryers.

Correspondence concerning this article should be addressed to M. A. Henson at mhenson@engin.umass.edu.

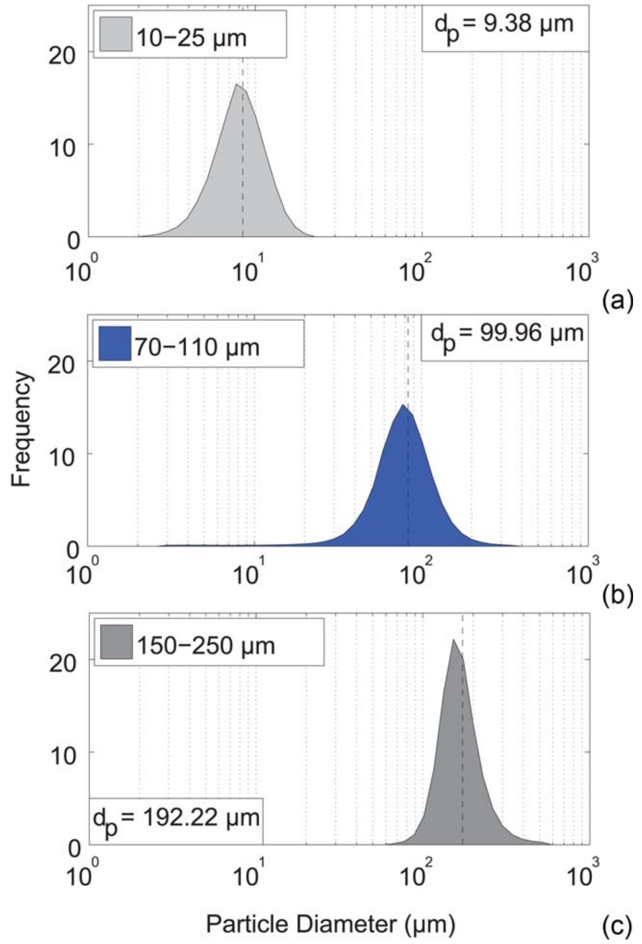

Figure 1. Particle-size distributions of the glass bead samples: (a) 10–25 μm, (b) 70–110 μm, and (c) 150–250 μm.

The dashed line indicates the volume-weighted mean diameter (d_p). [Color figure can be viewed in the online issue, which is available at wileyonlinelibrary.com.]

Materials and Methods

Experiments

Materials. The solids used for experiments were spherical glass beads (Corpuscular, Cold Spring, NY) of three size ranges: (a) 10–25 μm, (b) 70–110 μm, and (c) 150–250 μm. Particle-size distributions (PSDs) were measured with a HORIBA LA-920 static laser scattering analyzer (Albany, NY). Only this method was used to measure the particle size as it provides a good estimate for volume-based PSD. In addition, the method also provides sufficient information to characterize the glass bead samples. Figure 1 shows the measured PSDs as well as the volume weighted arithmetic mean diameters of the three bead samples. All the samples produced unimodal PSDs. Interestingly, the measured mean diameter of the 10–25 μm bead sample was 9.38 μm, which was outside the range claimed by the manufacturer.

Acetone was used as the solvent in all experiments. Important properties of acetone with respect to its vaporization behavior are listed in Table 1. The enthalpy of vaporization does not change significantly over the range of operating pressures considered in this work.

Table 1. Properties of Acetone at Different Operating Pressures

Solvent	Pressure (Torr)	Boiling Point[10] (°C)	Enthalpy of Vaporization (J/kg)	Molecular Weight[10] (g/mol)
Acetone	30	−15.39	5.67×10^5	58.08
	40	−10.47		
	50	−6.50		

Laboratory-Scale Vacuum Drying System. We designed and constructed a customized vacuum contact dryer system to perform our laboratory experiments (Figure 2). The oven was specially designed for efficient heat transfer to the cake and insulated to avoid heat loss. Rather than use electrical heaters on the walls of the oven, the cake was heated with a hot fluid that circulated through the tray upon which the sample dish was placed. The fluid temperature was regulated by a Lauda Model Proline RP 845 temperature controller (Delran, NJ) with an accuracy of 0.01°C. Nitrogen (purity 99.998%) was pumped into the oven as the carrier gas at a volumetric flow rate of 5 LPM (8.33×10^{-5} m^3/s). The nitrogen flow rate was regulated by a Cole Parmer Model 32907-69 flow controller (Vernon Hills, IL) with an accuracy of 0.1%. Gas in the oven head space consisting of evaporated solvents, nitrogen, and residual oxygen and carbon dioxide was continuously removed to maintain the oven pressure at the set point value. The exit gas flow rate was measured with an Omega Model FMA-1610A-VOL flow meter (Stamford, CT) with a maximum flow rate of 100 LPM (1.67×10^{-3} m^3/s) and an accuracy of 1%. The flow meter used the Hagen–Poiseuille equation to calculate the flow rate and was calibrated using pure nitrogen. Data from the flow controller and flow meter were logged using PuTTY (open source software under the MIT license). To enhance mixing of gases, the inlet and outlet gas ports were placed at the lower bottom right corner and the top of the oven, respectively. At the inlet flow rate of 5 LPM (8.33×10^{-5} m^3/s), the oven residence time (τ) was calculated to be 512 s by performing a nitrogen step experiment and fitting the nitrogen mass fraction data to the first-order differential equation .[11]

The oven pressure was regulated with a BUCHI Model V-850 pressure controller (New Castle, DE) that manipulated a control valve on the exit gas stream. The pressure controller operated as an on-off type controller with a specified tolerance of 1 Torr. Pressure data were logged using Distillation Record software provided by BUCHI. The exist gas was passed through a FTS Systems Model Titan Trap vapor trap (Warminster, PA) and then was removed from the system with an Edwards Model XDS10 A72601906 pump (Sanborn, NY). Three Oakton Model 073098B-K-G-12 type K thermocouples (Vernon Hills, IL) were available for direct placement inside the drying cake to measure spatial temperature gradients. The adjustable thermocouples were placed at 0, 0.8, and 1.8 cm from the base of the sample dish, and temperature data were recorded with a Cole-Parmer Model USB-5201 data logger (Vernon Hills, IL) using Tracer DAQ software provided by Cole-Palmer. Gas exiting the top of the oven through a tube wrapped in heat tape to avoid condensation of solvents was passed to an Extrel CMS Model Max LG 300 mass spectrometer (MS, Pittsburgh, PA) for composition analysis. The MS was capable of achieving an accuracy of 100 ppb (10^{-7} mole fraction) in the absence of interference between the components. Due to the presence of some interference, an accuracy of 10^{-5} was attainable after calibration. Mole fraction

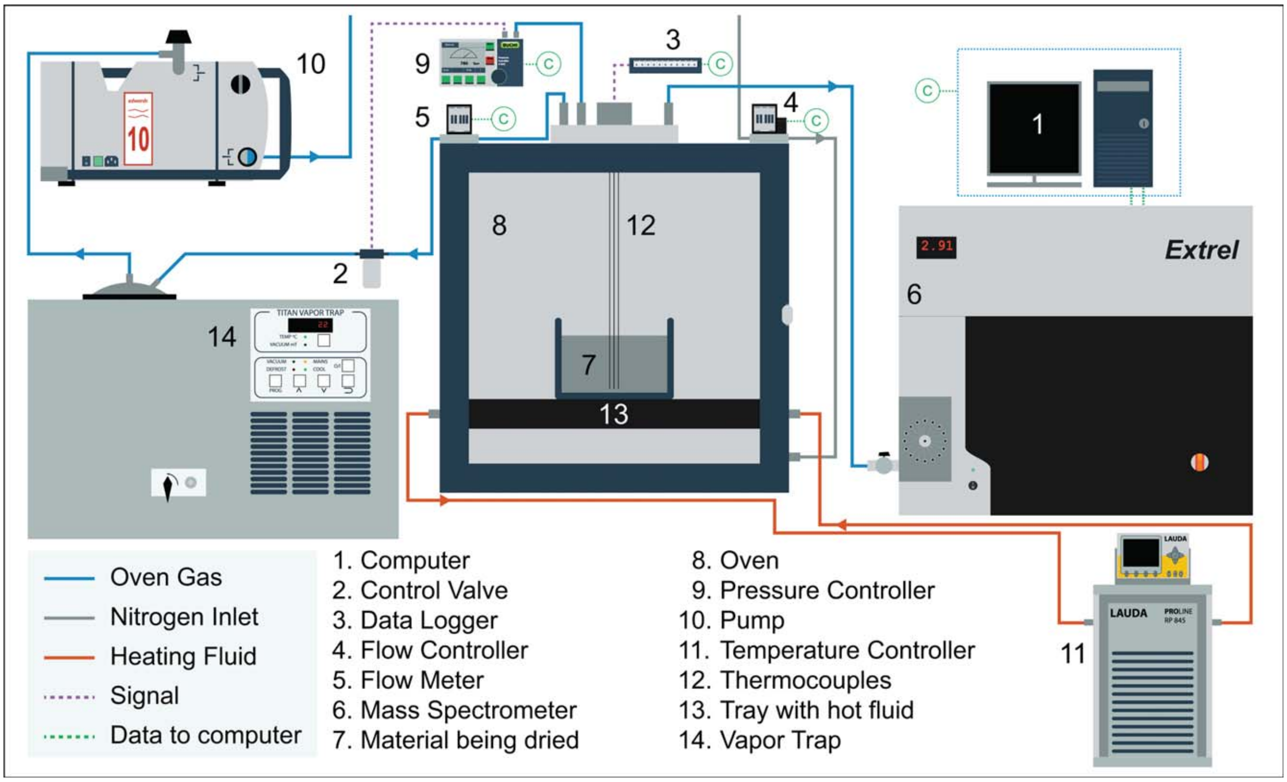

Figure 2. Laboratory-scale vacuum contact dryer connected to a portable MS for real-time analysis of drying performance.

[Color figure can be viewed in the online issue, which is available at wileyonlinelibrary.com.]

measurements were generated every 3–4 s and processed using Questor5 software provided by Extrel.

Procedure. The solid material was placed inside a glass dish with an inner diameter of 8.6 cm (OD: 9 cm) such that the cake thickness was 2.3 cm. The solid was saturated with the solvent, placed in the oven and outfitted with the three thermocouples. The vapor trap, pump, flow meter, flow controller, and thermocouple data loggers were turned on and data recording was initiated. The oven was closed securely and pressure reduction was commenced by opening the exit gas control valve using the pressure controller. This point represented time zero and was used to synchronize all data. Drying operation was stopped by venting the oven with air when the MS displayed a mole fraction of 0.5% or less of the least volatile component.

Multiphase transport model

Information Flow Diagram. Figure 3 shows the flow of information as the model was executed. The main components

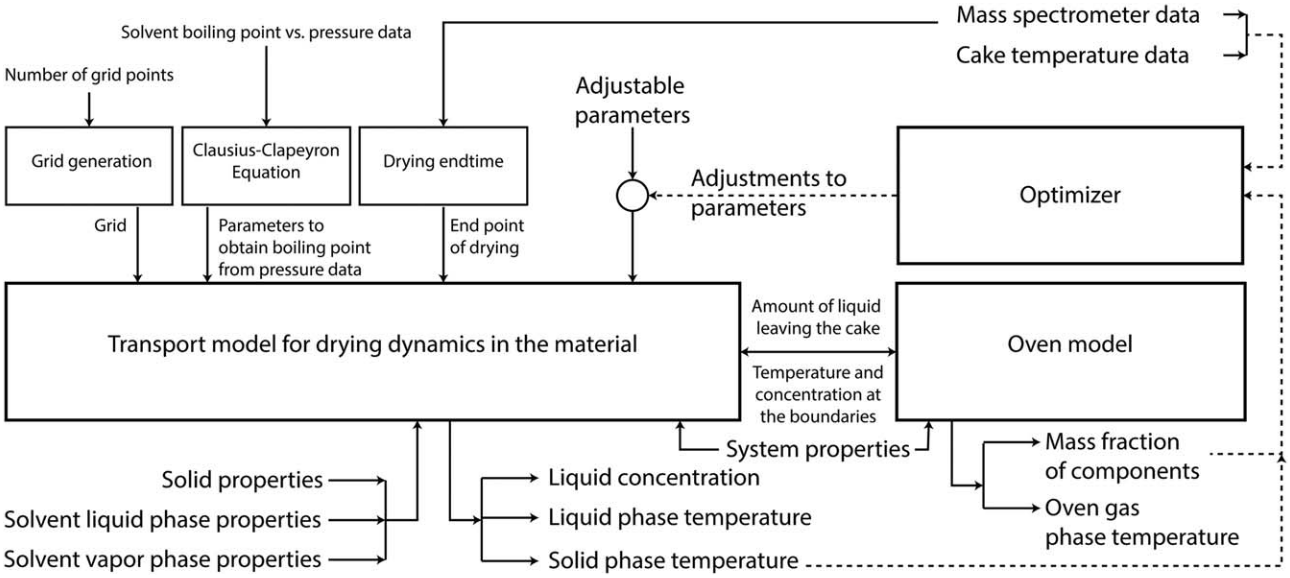

Figure 3. Information flow diagram for transport modeling and parameter estimation.

The dashed lines represent flow of data used by the optimizer for parameter estimation.

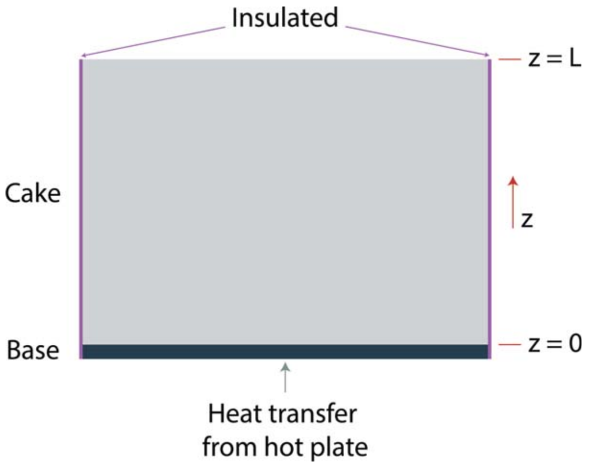

Figure 4. Schematic for derivation of the cake drying model.

[Color figure can be viewed in the online issue, which is available at wileyonlinelibrary.com.]

were the multiphase transport model (MPTM), grid generation module, oven model, drying time endpoint module, and optimizer module. The MPTM was supplied solid properties and liquid and vapor phase properties of the solvent. Grid generation was a simple module that generated a spatial grid for numerical solution given the thickness of the cake and the specified number of nodes. The Partial Differential Equations (PDEs) were discretized in space along this grid. The time-dependent Ordinary Differential Equations (ODEs) obtained from this discretization procedure were solved in the MPTM. The Clausius–Clapeyron equation was used to calculate the enthalpy of vaporization for use in the MPTM module using pressure and boiling point data.[10] A drying time module[11] was used to detect the endpoint of drying, at which time the simulation was terminated. Under assumption that the gas head space was well mixed, the oven model received the solvent vaporization rate from MPTM and calculated the gas compositions leaving the oven. Both the MPTM and the oven module were supplied with system properties such as the sample container dimensions, the oven headspace volume, and so forth. Following one or more simulations, outputs from both the MPTM and the oven model were sent to the optimizer where measured and predicted variables were compared based on a specified least-squares objective function. Updated values of selected model parameters for future simulations were generated by minimizing the objective function.

Governing Equations for Cake Drying Model. In this analysis, the macroscopic continuum approach was adopted. The model accounted for two phases, the liquid phase and a combined solid-vapor phase. We assumed that the vapor phase would very rapidly track the temperature of the solid phase. The characteristic time for temperature to reach equilibrium between the vapor and solid phases was approximated as the time constant for heat transfer in the vapor phase. This time constant was of the order 10^{-3} s for the system under consideration. As the drying time was many orders of magnitude larger, the lumping of the solid and vapor phase for the heat balance was valid. When conditions were favorable for boiling, the temperature of the liquid phase was constrained to be equal to the saturation temperature as observed in our experiments. However, this constraint was not imposed on the solid-vapor phase. All variables in the model varied in time and only in the z direction spatially (Figure 4). Variables were volume averaged using the approach described by Whitaker.[3] For example, in a control volume V containing solid, liquid, and vapor, the average concentration of solvent in the liquid was $C_l = \frac{1}{V}\int C_{l,\mathrm{local}} dV$. Thus, $C_{l,\mathrm{local}}$ is treated as the solvent concentration in the liquid at any point in the control volume V.

The model was derived based on the following assumptions,

1. Mass transfer in the liquid phase occurred via diffusion, and the diffusion coefficient varied linearly with the moisture content as shown in Eq. 2. The resulting diffusion equation was of the form of the Richard's equation.
2. All material properties were treated as constants including $k_s, k_l, k_v, c_{p_s}, c_{p_l}, c_{p_v}, c_{p_b}, \Delta H, \rho_l, \rho_s,$ and ρ_b (see Notation).
3. Mass-transfer resistance for vapor flow from the point of vaporization to the head space of the oven was negligible.
4. The vapor behaved like an ideal gas under the vacuum conditions used. Hence, the density of the vapor was calculated from the ideal gas equation.
5. Boiling was the only form of vaporization considered in the model, with evaporation assumed to be negligible. When the temperature of the liquid phase was equal to or greater than the saturation temperature, the liquid was considered to be boiling.
6. The solid was impermeable to the liquid and vapor and any form of adsorption on the solid particles was neglected.
7. The liquid phase was considered to be incompressible.
8. The effect of the size of the solid particles on drying behavior could be captured with the mean particle diameter independent of the PSD.
9. Deformation of the porous medium was considered to be negligible.
10. The sides of the cake were considered to be perfectly insulated (Figure 4). Hence, heat transfer in the radial direction was omitted.
11. Diffusion of gas from the oven head space into the cake was considered to be negligible. This assumption was based on the fact that boiling leads to high volumes of vapor being generated. Because the cake was initially saturated with solvent, this assumption was the potential to introduce significant error only at the very end of the drying cycle. However, the ppm concentration of the solvent at this point was much lower than the acceptable residual solvent concentration (e.g., see Ref. 12 for acetone). Therefore, the simulation was typically stopped before this point was reached.

Mass Balance on the Liquid Phase. Based on the assumptions above, the mass balance on the liquid phase had the form in Eq. 1. The diffusion coefficient varied linearly with the liquid volume fraction, denoted by ϵ_l, as shown in Eq. 2. Here, D_o is the diffusion coefficient when the void space was saturated with liquid. As the equations were volume averaged, the linear reduction in the diffusion coefficient D with volume fraction ϵ_l represented a reduction in the cross-sectional area available for diffusion. In Eq. 1, $\dot{\Gamma}$ denotes the rate of liquid mass vaporizing per unit volume. For the case of drying by evaporation, this rate has been replaced with various empirical forms.[1] In this work, we rigorously calculated the rate from an energy balance on the liquid phase

$$\frac{\partial C_l}{\partial t} = \frac{\partial}{\partial z}\left(D\frac{\partial C_l}{\partial z}\right) - \dot{\Gamma} \tag{1}$$

Table 2. Volume Fraction, Concentrations, and Thermal Conductivities of the Different Phases

Component	Volume Fraction	Concentration (kg/m^3)	Thermal Conductivity (W/m K)
Solid	$\epsilon_{\mathrm{s}}=1-\epsilon_{\mathrm{void}}$	$C_{\mathrm{s}}=\rho_{\mathrm{s}}\epsilon_{\mathrm{s}}$	$\bar{k}_{\mathrm{s}}=k_{\mathrm{s}}\epsilon_{\mathrm{s}}$
Liquid	$\epsilon_{\mathrm{l}}=\epsilon_{\mathrm{void}}-\epsilon_{\mathrm{v}}$	$C_{\mathrm{l}}=\rho_{\mathrm{l}}\epsilon_{\mathrm{l}}$	$\bar{k}_{\mathrm{l}}=k_{\mathrm{l}}\epsilon_{\mathrm{l}}$
Vapor	ϵ_{v}	$C_{\mathrm{v}}=\rho_{\mathrm{v}}\epsilon_{\mathrm{v}}=\frac{PM_{\mathrm{v}}}{R_{\mathrm{g}}T_{\mathrm{sv}}}\epsilon_{\mathrm{v}}$	$\bar{k}_{\mathrm{v}}=k_{\mathrm{v}}\epsilon_{\mathrm{v}}$
Total	$\epsilon_{\mathrm{s}}+\epsilon_{\mathrm{l}}+\epsilon_{\mathrm{v}}=1$	–	–

$$D=D_o\epsilon_{\mathrm{l}} \tag{2}$$

Mass Balance on the Solid-Vapor Phase. The concentration of solid was assumed to be constant in time and space. Hence

$$\frac{\partial C_{\mathrm{s}}}{\partial t}=0 \tag{3}$$

Furthermore, newly created vapor was assumed to have a free path from its point of origin within the cake to the oven head space. Exploiting this assumption to simplify the calculations, we used the fact that $\epsilon_{\mathrm{v}}=1-(\epsilon_{\mathrm{s}}+\epsilon_{\mathrm{l}})$ as listed in Table 2.

Energy Balance on the Liquid Phase. Four distinct mechanisms were considered to affect the rate of change of enthalpy in the liquid phase. As shown in Eq. 4, these mechanisms were heat transfer by conduction, heat transfer due to diffusion, heat transferred from the solid-vapor phase, and enthalpy lost due to vaporization

$$\underbrace{\frac{\partial(C_{\mathrm{l}}h_{\mathrm{l}})}{\partial t}}_{\substack{\text{Rate of change of}\\ \text{enthalpy of liquid}}}=\underbrace{\frac{\partial}{\partial z}\left(\bar{k}_{\mathrm{l}}\frac{\partial T_{\mathrm{l}}}{\partial z}\right)}_{\substack{\text{Heat transfer}\\ \text{by conduction}}}+\underbrace{\frac{\partial}{\partial z}\left(D\frac{\partial C_{\mathrm{l}}}{\partial z}h_{\mathrm{l}}\right)}_{\substack{\text{Heat transfer by}\\ \text{diffusion of liquid}}}+\underbrace{h_{\mathrm{int}}(T_{\mathrm{sv}}-T_{\mathrm{l}})}_{\substack{\text{Heat transfered from}\\ \text{solid-vapor phase}}}-\underbrace{\dot{\Gamma}h_{\mathrm{v}}}_{\substack{\text{Enthalpy lost due}\\ \text{to vaporization}}} \tag{4}$$

Using Eq. 1, the energy balance Eq. 4 can be simplified as

$$\left(C_{\mathrm{l}}c_{p_{\mathrm{l}}}\right)\frac{\partial T_{\mathrm{l}}}{\partial t}=\frac{\partial}{\partial z}\left(\bar{k}_{\mathrm{l}}\frac{\partial T_{\mathrm{l}}}{\partial z}\right)+h_{\mathrm{int}}(T_{\mathrm{sv}}-T_{\mathrm{l}})-\dot{\Gamma}\Delta H+\underbrace{Dc_{p_{\mathrm{l}}}\frac{\partial C_{\mathrm{l}}}{\partial z}\frac{\partial T_{\mathrm{l}}}{\partial z}}_{\textbf{neglected}} \tag{5}$$

When conditions were favorable for boiling, we attempted to mimic our experimental results by constraining the liquid temperature T_{l} to track the saturation temperature T_{sat} calculated at the current pressure. Hence, Eq. 5 was rearranged to obtain an explicit equation for $\dot{\Gamma}$ as shown in Eq. 6

$$\dot{\Gamma}=\frac{\frac{\partial}{\partial z}\left(\bar{k}_{\mathrm{l}}\frac{\partial T_{\mathrm{l}}}{\partial z}\right)+h_{\mathrm{int}}(T_{\mathrm{sv}}-T_{\mathrm{l}})-\left(C_{\mathrm{l}}c_{p_{\mathrm{l}}}\right)\frac{\partial T_{\mathrm{sat}}}{\partial t}}{\Delta H} \tag{6}$$

The term $Dc_{p_{\mathrm{l}}}\frac{\partial C_{\mathrm{l}}}{\partial z}\frac{\partial T_{\mathrm{l}}}{\partial z}$ was neglected as it was very small compared to the other terms. When the liquid started boiling, the temperature in the liquid phase was held constant at the saturation temperature. This constraint led to the condition $\frac{\partial T_{\mathrm{l}}}{\partial z}\approx 0$.

The term $h_{\mathrm{int}}(T_{\mathrm{sv}}-T_{\mathrm{l}})$ in Eq. 6 was based on Newton's law of cooling and represented the heat flux to the liquid phase from the solid-vapor phase. The heat transfer coefficient h_{int} was calculated from the expression in Eq. 7, where α is the specific surface area of the solid particles. As the particles under consideration are assumed to be perfectly spherical, $\alpha=\frac{6}{d_p}$, where d_p is the mean particle diameter. Also, β was calculated using a function that defined the fraction of surface area of the solid phase in contact with the liquid phase (Eq. 8) where, ϵ_{crit} is the volume fraction of liquid after which the liquid does not wet the surface of the solid completely. The value $\epsilon_{\mathrm{crit}}=0.2672$ was obtained from the geometry of a body centered cubic packing structure.

$$h_{\mathrm{int}}=\alpha\epsilon_{\mathrm{s}}\beta h_{\mathrm{sv-l}} \tag{7}$$

$$\beta=\begin{cases}1, & \text{if } \epsilon_{\mathrm{l}}\geq\epsilon_{\mathrm{crit}}\\ -\left(\dfrac{\epsilon_{\mathrm{l}}}{\epsilon_{\mathrm{crit}}}\right)^2+2\left(\dfrac{\epsilon_{\mathrm{l}}}{\epsilon_{\mathrm{crit}}}\right), & \text{if } \epsilon_{\mathrm{l}}<\epsilon_{\mathrm{crit}}\end{cases} \tag{8}$$

Energy Balance on the Solid-Vapor Phase. In the solid-vapor phase, heat is transferred primarily through conduction and heat is lost to the liquid phase by convective transfer as shown in Eq. 9. Heat transferred due to diffusion of vapor given by $D_{\mathrm{v}}c_{p_{\mathrm{v}}}\frac{\partial C_{\mathrm{v}}}{\partial z}\frac{\partial T_{\mathrm{sv}}}{\partial z}$ was neglected as it was three orders of magnitude smaller than the dominant terms. Also, the term $\dot{\Gamma}$ $c_{p_{\mathrm{v}}}(T_{\mathrm{sv}}-T_{\mathrm{l}})$ was neglected as $h_{\mathrm{int}}\gg\dot{\Gamma}c_{p_{\mathrm{v}}}$. These simplifications reduced model complexity and improved reduced simulation efficiency. The average conductivity of the solid-vapor phase was given by $\bar{k}_{\mathrm{sv}}=\bar{k}_{\mathrm{s}}+\bar{k}_{\mathrm{v}}$

$$\begin{aligned}\left(C_{\mathrm{s}}c_{p_{\mathrm{s}}}+C_{\mathrm{v}}c_{p_{\mathrm{v}}}\right)\frac{\partial T_{\mathrm{sv}}}{\partial t}&=\frac{\partial}{\partial z}\left(\bar{k}_{\mathrm{sv}}\frac{\partial T_{\mathrm{sv}}}{\partial z}\right)-h_{\mathrm{int}}(T_{\mathrm{sv}}-T_{\mathrm{l}})\\&\quad-\underbrace{\dot{\Gamma}c_{p_{\mathrm{v}}}(T_{\mathrm{sv}}-T_{\mathrm{l}})}_{\textbf{neglected}}+\underbrace{D_{\mathrm{v}}c_{p_{\mathrm{v}}}\frac{\partial C_{\mathrm{v}}}{\partial z}\frac{\partial T_{\mathrm{sv}}}{\partial z}}_{\textbf{neglected}}\end{aligned} \tag{9}$$

Energy Balance on the Base Layer. The base layer, which was defined as the bottom of the dish between the cake and the heated plate, transfer heat via convection

$$\begin{gathered}\rho_{\mathrm{b}}c_{p_{\mathrm{b}}}\frac{\partial T_{\mathrm{b}}}{\partial t}=\dot{q}_{\mathrm{in}}-\dot{q}_{\mathrm{out}}\\ \dot{q}_{\mathrm{in}}=h_t(T_{\mathrm{f}}-T_{\mathrm{b}})\\ \dot{q}_{\mathrm{out}}=h_{\mathrm{b}}\epsilon_{\mathrm{l}}(t,z=0)(T_{\mathrm{b}}-T_{\mathrm{l}}(t,z=0))\\ +h_{\mathrm{b}}(\epsilon_{\mathrm{s}}(t,z=0)+\epsilon_{\mathrm{v}}(t,z=0))(T_{\mathrm{b}}-T_{\mathrm{sv}}(t,z=0))\end{gathered} \tag{10}$$

Here, h_t is the heat-transfer coefficient that accounts for heat flux from the hot fluid to the base layer, and h_{b} represents the heat-transfer coefficient between the base layer and the first layer of particles. The first layer of particles is considered to show different properties than the other particles in the cake as discussed elsewhere.[13]

Initial Conditions. The cake was considered to be completely saturated with liquid at $t = 0$. This condition matched the initial state of the cake used in our experiments. The liquid phase temperature T_l and the solid-vapor phase temperature T_{sv} were both obtained from data at $t = 0$ using interpolation (Eq. 12). The initial condition for the temperature of the base layer T_b was obtained by extrapolating from temperature data. The interpolation and extrapolation methods are discussed in Section Numerical Methods

$$\epsilon_l(t=0,z)=\epsilon_{void} \tag{11}$$

$$\begin{aligned} T_l(t=0,z)&=T_{sv}(t=0,z)\\ &=\text{Interpolate}(T_{data}) \end{aligned} \tag{12}$$

$$T_b(t=0)=\text{Extrapolate}(T_{data}) \tag{13}$$

The solid volume fraction was obtained from experimental data using Eq. 14, where m_l is the mass of liquid used to saturate the cake and V_c is volume of the cake. The cake volume was obtained from the thickness (L) and the cross-sectional area (A_c) of the cake using Eq. 15. The average density of the solid was obtained from Eq. 16

$$\epsilon_s=1-\frac{m_l}{\rho_l V_c} \tag{14}$$

$$V_c=L\cdot A_c \tag{15}$$

$$\rho_s=\frac{m_s}{\epsilon_s V_c} \tag{16}$$

$$\epsilon_{void}=1-\epsilon_s$$

Boundary Conditions. The flux of liquid at the cake boundaries was set equal to 0 (Eq. 17). For both the liquid and solid-vapor phases, heat was transferred from the base layer and lost to the oven head space via convection (Eqs. 18 and 19)

$$-D\frac{\partial C_l}{\partial z}=\begin{cases} 0, & z=0\\ 0, & z=L \end{cases} \tag{17}$$

$$-\bar{k}_l\frac{\partial T_l}{\partial z}=\begin{cases} h_b\epsilon_l(T_b-T_l), & z=0\\ h_{oven}\epsilon_l(T_l-T_{oven}), & z=L \end{cases} \tag{18}$$

$$-\bar{k}_{sv}\frac{\partial T_{sv}}{\partial z}=\begin{cases} h_b\epsilon_{sv}(T_b-T_{sv}), & z=0\\ h_{oven}\epsilon_{sv}(T_{sv}-T_{oven}), & z=L \end{cases} \tag{19}$$

Governing Equations for the Oven Model. The gas flows into the oven gas phase are the nitrogen purge gas and evaporating solvent from the cake. The oven has one outlet flow to the pump (Figure 2). The following assumptions were invoked to derive the oven model

1. The vapor behaved like an ideal gas so the vapor density could be calculated from the ideal gas equation.
2. The gas phase was well mixed.
3. The gas phase had no heat transferred via conduction or convection. Therefore, changes in enthalpy were only due to gas flow into and out of the control volume.

Mass Balances on the Oven Gas Phase. An overall mass balance on the gas phase in the oven yielded

$$\frac{dm}{dt}=\dot{m}_{purge}+\dot{m}_{sol}-\dot{m}_{out} \tag{20}$$

Table 3. Initial Guesses and Allowable Ranges for the Adjustable Model Parameters

Parameter	Initial Guess	Lower Bound	Upper Bound
k_s (W/m K)	0.6	0.2	2
h_t (W/m^2 K)	120	1	200
h_{oven} (W/m^2 K)	10	1	100
D_o (m^2/s)	1e-6	5e-8	1e-5
h_{sv-1} (W/m^2 K)	0.5	0.01	10
h_b (W/m^2 K)	60	1	200

The mass balance for component "i" was solved for four out of the five components in the gas phase. The mass fraction of the fifth component (CO_2) was obtained using Eq. 22

$$\frac{d(mx_i)}{dt}=\dot{m}_{i,in}-\dot{m}_{out}x_i \tag{21}$$

$$\sum x_i=1 \tag{22}$$

$$\dot{m}_{i,in}=\begin{cases} \dot{m}_{purge}, & i\equiv N_2\\ \dot{m}_{sol}, & i\equiv \text{sol}\\ 0, & \text{otherwise} \end{cases}$$

The unknown term $\dot{m}_{out}$ was eliminated by combining Eqs. 20 and 21

$$m\frac{d(x_i)}{dt}=\dot{m}_{i,in}-\left(\dot{m}_{purge}+\dot{m}_{sol}\right)x_i \tag{23}$$

Energy Balance on Oven Gas Phase. An energy balance on the gas phase in the oven yielded

$$\frac{d(mh)}{dt}=\dot{m}_{purge}h_{purge}-\dot{m}_{out}h_{out}+\dot{m}_{sol}h_{sol} \tag{24}$$

By substituting Eq. 20 into Eq. 24, the following equation was obtained

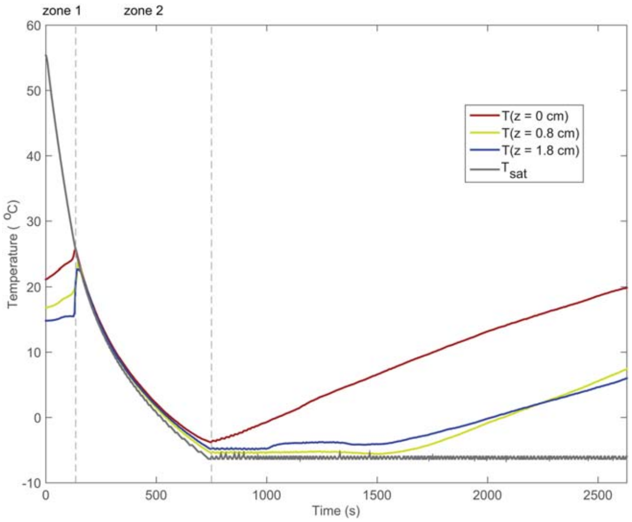

Figure 5. Temperature data from the three thermocouples and T_{sat} calculated from pressure data.

Operating conditions were particle size: 70–110 μm, temperature: 40°C, and pressure: 50 Torr (6.66 kPa). [Color figure can be viewed in the online issue, which is available at wileyonlinelibrary.com.]

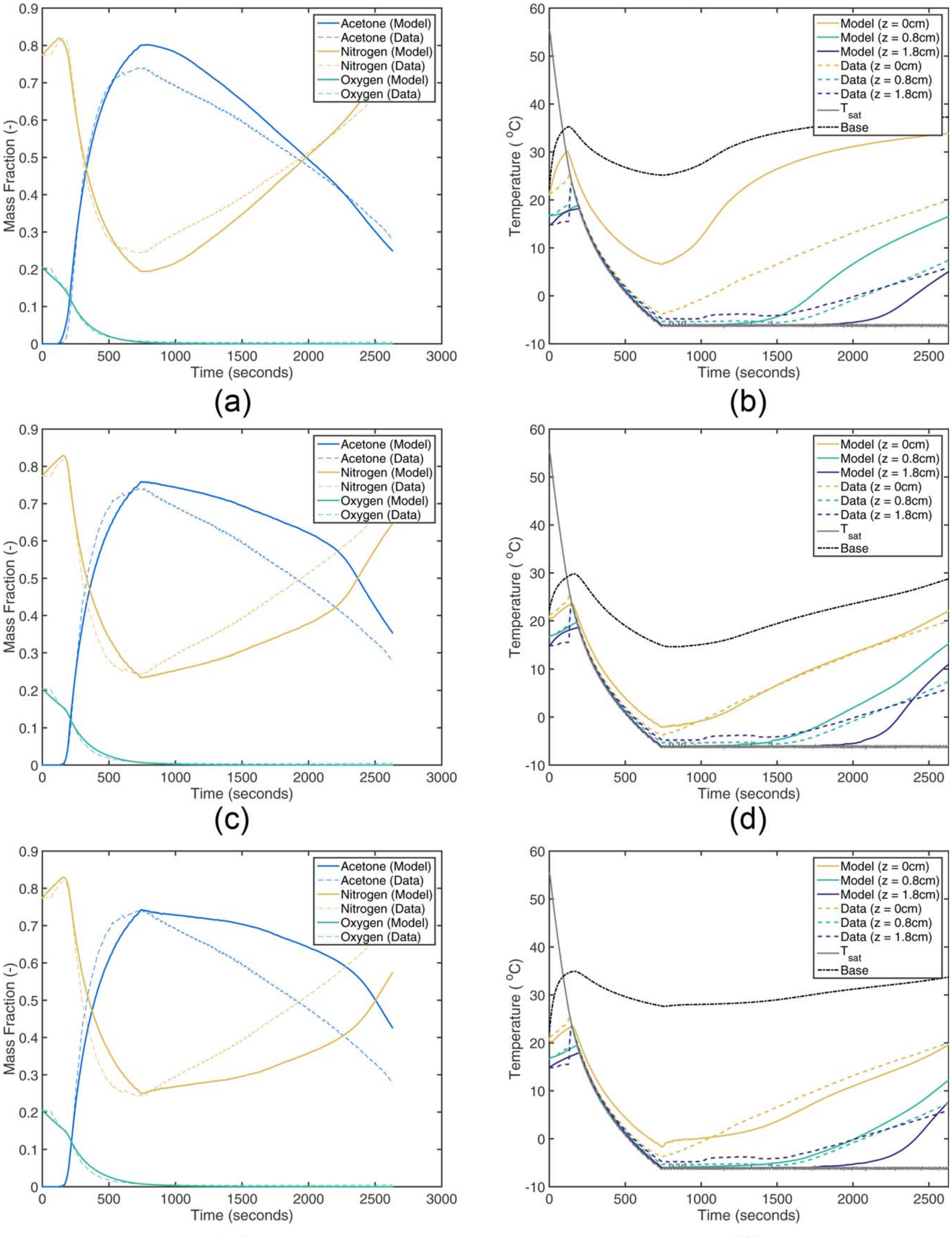

Figure 6. Comparison of MS data and oven headspace composition predictions on the left and temperature data with solid-vapor phase temperature predictions on the right.

Objective functions involved composition data only (χ_{MS}), both composition and temperature data ($\chi_{MS}+\chi_T$) and temperature data only (χ_T). Operating conditions were a particle size range of 70–110 μm, temperature of 40°C, and pressure of 50 Torr (6.66 kPa). [Color figure can be viewed in the online issue, which is available at wileyonlinelibrary.com.]

Table 4. Estimated Parameters Obtained Using Different Objective Functions

Optimization Type	k_s (W/m K)	h_t (W/m^2 K)	h_{oven} (W/m^2 K)	D_o (m^2/s)	$h_{\text{sv}-1}$ (W/m^2 K)	h_b (W/m^2 K)
MS	0.20	141.47	1.24	2.62 E −06	3.34	145.77
MS and T	0.99	59.47	57.21	2.21 E −06	8.92	91.59
T	1.07	116.97	16.86	2.42 E −06	4.13	49.99

These values correspond to the results shown in Figure 6.

$$mc_{p_{\text{avg}}}\frac{dT_{\text{oven}}}{dt}=\dot{m}_{\text{purge}}\left(c_{p_{\text{purge}}}T_{\text{purge}}-c_{p_{\text{avg}}}T_{\text{oven}}\right)+\dot{m}_{\text{sol}}\left(c_{p_{\text{v}}}T_{\text{sv}}(t,z{=}L)-c_{p_{\text{avg}}}T_{\text{oven}}\right) \tag{25}$$

Here, $c_{p_{\text{avg}}}$ is the average specific heat capacity of the gas phase given by $c_{p_{\text{avg}}}=\sum c_{p_i}x_i$, T_{purge} was obtained from the flow controller data, andi$\dot{m}_{\text{sol}}$ was calculated as

$$\dot{m}_{\text{sol}}=\frac{1}{L}\int_0^L\left(\frac{\partial C_1}{\partial t}+\frac{\partial C_{\text{v}}}{\partial t}\right)dz \tag{26}$$

Initial Conditions. Initial conditions for the mass fractions were interpolated using data obtained from the MS. The mole fractions provided by the MS were converted to mass fractions and then interpolation to obtain mass fractions at $t=0$. The initial condition for T_{oven} was interpolated using the temperature data from the flow controller

$$x_i(t{=}0)=\text{Interpolate}(x_{\text{MS}-\text{data}}) \tag{27}$$

$$T_{\text{oven}}(t{=}0)=\text{Interpolate}(T_{\text{FC}-\text{data}}) \tag{28}$$

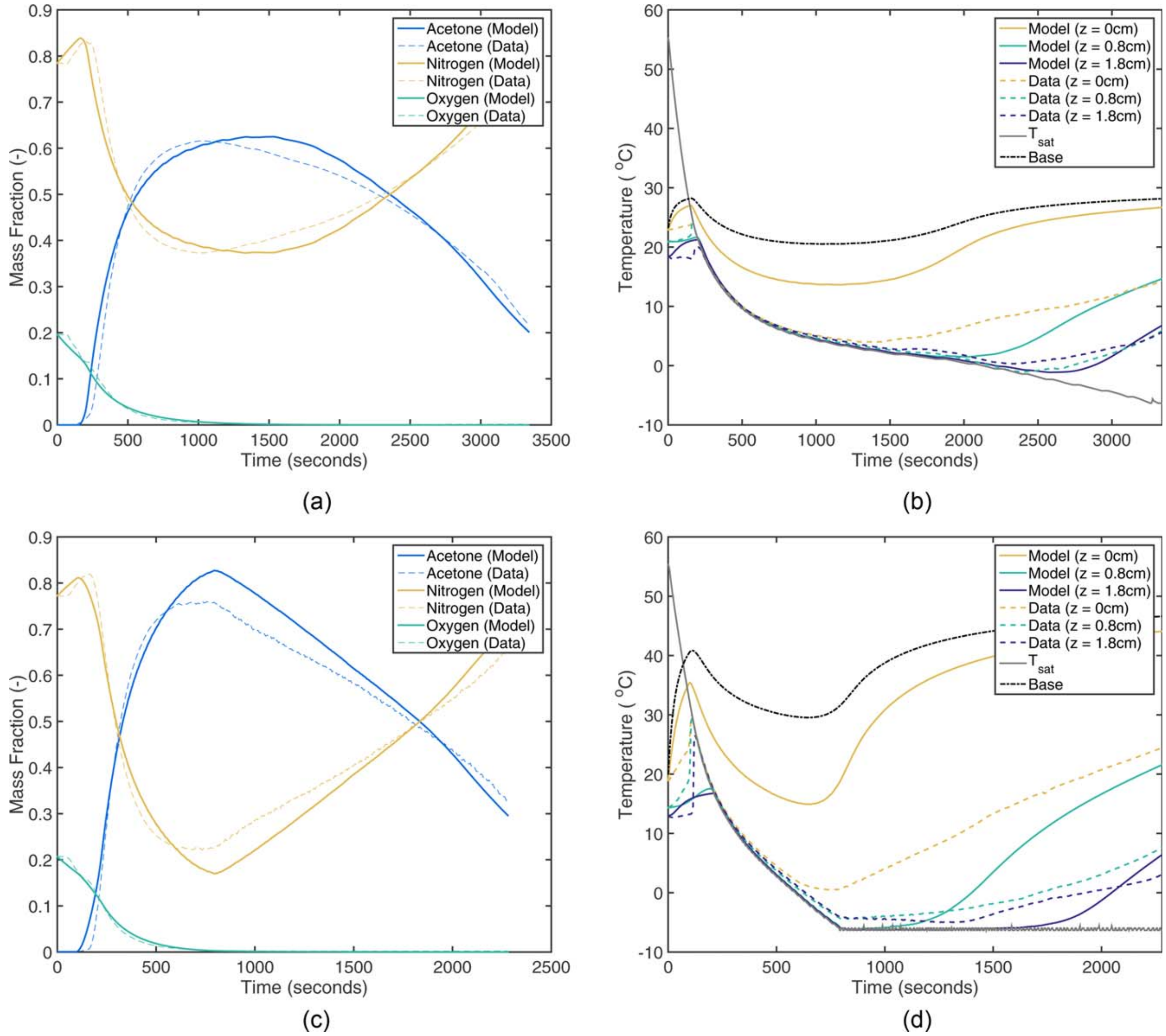

Figure 7. Comparison of MS data and oven headspace composition predictions on the left and temperature data with solid-vapor phase temperature predictions on the right.

Operating conditions were a particle size range of 70–110 μm and pressure of 50 Torr (6.66 kPa). [Color figure can be viewed in the online issue, which is available at wileyonlinelibrary.com.]

Numerical methods

Model Simulation. The complete MPTM consisted of a set of partial differential equations in time t and the axial cake coordinate z. The model was solved by discretizing the cake spatial domain using the finite volume method with N nodes, such that each node corresponded to an element of thickness dz. Therefore, $L=N \cdot dz$ with the cake thickness $L=2.3 \times 10^{-2}$ for all cases studied. Spatial derivatives were approximated using central difference formulas with accuracy of $O(dz)^2$. We found that $N=23$ nodes ($dz=10^{-3}$) provided sufficient accuracy of $O\left(10^{-6}\right)$ given that the error in our MS data was three orders of magnitude larger. Grid dependency tests showed that nearly converged solutions were obtained with 23 nodes, and that the main impact of further increases in N was to increase the simulation time. The chosen grid allowed a single simulation to be completed within 30 s, which was important to reduce the computational effort for parameter estimation.

The ODEs obtained after spatial discretization of the cake equations were combined with the ODEs from the oven model to generate a large nonlinear ODE system which was integrated forward in time. The ratio of time scales of heat and mass transfer provided a reasonable estimate of the system stiffness. Because this ratio was approximately 10, we used the MATLAB solver *ode23t* specifically designed for moderately stiff problems while avoiding numerical damping. We found that stiff MATLAB solvers were not able to efficiently solve the model because the use of pressure data to calculate the time derivative of liquid temperature introduced high frequency noise into equations.

Initial conditions for temperatures in the cake and the base layer were obtained from interpolation and extrapolation of thermocouple data, respectively. The MATLAB function **interp1** with the *extrap* option was used for this purpose. To avoid numerical problems, a small penalty was added to ϵ_l such that $\epsilon_l(t=0,z)=\epsilon_{\text{void}}-10^{-6}$.

Parameter Estimation. The MPTM contained a number of parameters that could not be directly obtained from the literature and/or were expected to change with particle size and dryer

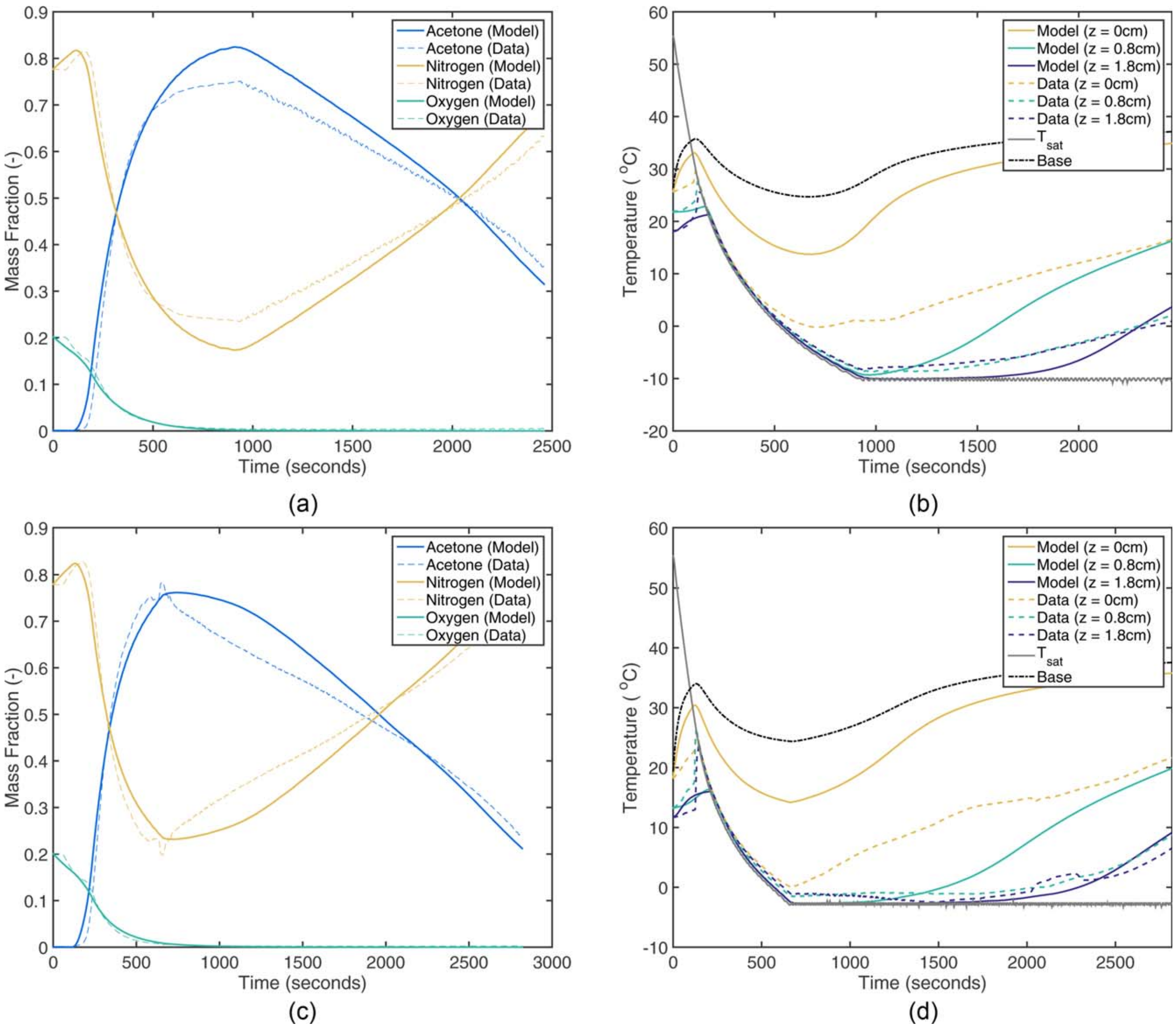

Figure 8. Comparison of MS data and oven headspace composition predictions on the left and temperature data with solid-vapor phase temperature predictions on the right.

Operating conditions were a particle size range of 70–110 μm and temperature of 40°C. [Color figure can be viewed in the online issue, which is available at wileyonlinelibrary.com.]

operating conditions. These parameters were estimated from our drying data as explained below. The estimated parameters were: (1) the liquid diffusion coefficient when the cake is saturated D_o; (2) the thermal conductivity of the solid k_s; (3) the heat-transfer coefficient between the solid-vapor and liquid phases h_{sv-l}; (4) the heat-transfer coefficient between the heating fluid to the base layer h_t; (5) the heat-transfer coefficient between the base layer and the bottom of cake h_b; and (6) the heat-transfer coefficient between the top of cake and the oven headspace h_{oven}. We assumed that D_o, k_s, h_t, and h_{oven} would vary only with particle size. In a previous study on vacuum drying,[11] we showed that solvent profiles were much more strongly affected by particle size than operating temperature and pressure. These results suggested significant differences in the mass-transfer rates due to particle size. Because the diffusion coefficient D_o was the only parameter that directly affected mass transfer, D_o was considered to change only with particle size. The thermal conductivity k_s was not expected to vary significantly over the ranges of temperature[14] and pressure[15,16] considered in this work. We considered h_t to be a system property independent of the particular operating conditions. The boundary condition for heat transfer at the open end of the cake shows that h_{oven} should only vary with particle size. By contrast, both h_{sv-l} and h_b were expected to vary with temperature and pressure as well as the particle size due to their roles in capturing the very complex process of heat transfer due to boiling.[17,18]

The six adjustable parameters were estimated from composition and temperature data by minimizing least-squares objective functions penalizing the difference between the measured and predicted values. More specifically, predicted temperatures of the solid-vapor phase were compared to temperature data from the three thermocouples and predicted nitrogen and acetone mass fractions from the oven model were compared to data from the MS using the objective functions Eq. 29. Here, N is the number of data points in time available for comparison. We performed parameter estimation using temperature data alone (χ_T), composition data alone (χ_{MS}) and combined temperature-composition data ($\chi_{MS}+\chi_T$). The spatially

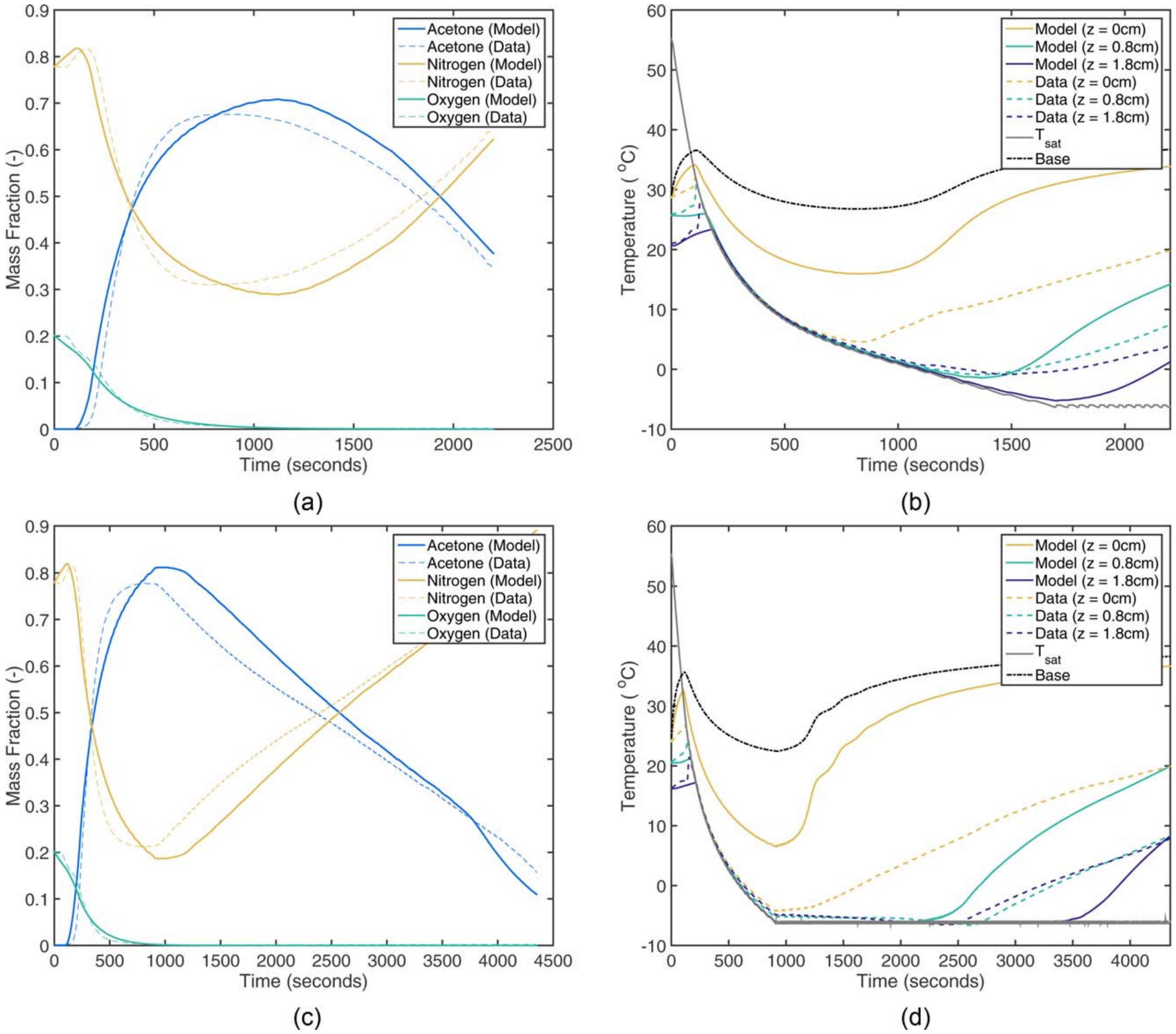

(a)

(b)

(c)

(d)

Figure 9. Comparison of MS data and oven headspace composition predictions on the left and temperature data with solid-vapor phase temperature predictions on the right.

Operating conditions were a temperature of 40°C and pressure of 50 Torr (6.66 kPa). [Color figure can be viewed in the online issue, which is available at wileyonlinelibrary.com.]

discretized model described above was posed as a set of equality constraints in the optimization problem, which was solved in MATLAB with the nonlinear least squares optimizer **lsqnonlin**. Because the optimization problem is nonconvex, we used the function **Multistart** in the global optimization toolbox to generate 15 locally optimal solutions for each case and selected the solution with the lowest objective function value

$$\chi_{\mathrm{MS}}=\sum_{j=\mathrm{N}_2,\mathrm{sol}}\sum_{i}^{N}\left(x_{i,j}^{\mathrm{model}}-x_{i,j}^{\mathrm{data}}\right)^2 \tag{29}$$

$$\chi_{T}=\sum_{j=1}^{3}\sum_{i}^{N}\left(\frac{T_{i,j}^{\mathrm{model}}-T_{i,j}^{\mathrm{data}}}{T_{\mathrm{f}}-T_{\mathrm{sat}}}\right)^2 \tag{30}$$

We used root mean squared (RMS) values defined in Eq. 31 for the mass fractions and in Eq. 32 for the temperatures as measures of the parameter fitting errors. The relation between RMS and χ values is $\chi=N\cdot\mathrm{RMS}^2$. Because they are based on normalized variables, the RMS values are reasonable measures of the relative percentage errors

$$\mathrm{RMS}_{\mathrm{MS}}=\sqrt{\frac{1}{N}\sum_{j=\mathrm{N}_2,\mathrm{sol}}\sum_{i}^{N}\left(x_{i,j}^{\mathrm{model}}-x_{i,j}^{\mathrm{data}}\right)^2} \tag{31}$$

$$\mathrm{RMS}_{T}=\sqrt{\frac{1}{N}\sum_{j=1}^{3}\sum_{i}^{N}\left(\frac{T_{i,j}^{\mathrm{model}}-T_{i,j}^{\mathrm{data}}}{T_{\mathrm{f}}-T_{\mathrm{sat}}}\right)^2} \tag{32}$$

The initial guess and allowable range of each parameter are shown in Table 3. The initial guesses for k_{s}, h_t, and h_{oven} were obtained by running the optimizer to match the three temperatures after the cake was dry using data collected for 70–110 μm beads at 40 °C and 50 Torr (6.66 kPa). Initial guesses for $h_{\mathrm{sv}-1}$ and h_{b} were obtained by fitting the same dataset by trial and error to achieve approximate agreement with the model. The initial value of h_{b} was set to be half that of h_t.

Results and Discussion

Experimental results

Figure 5 shows temperature data collected at the three points in the cake along with the saturation temperature of

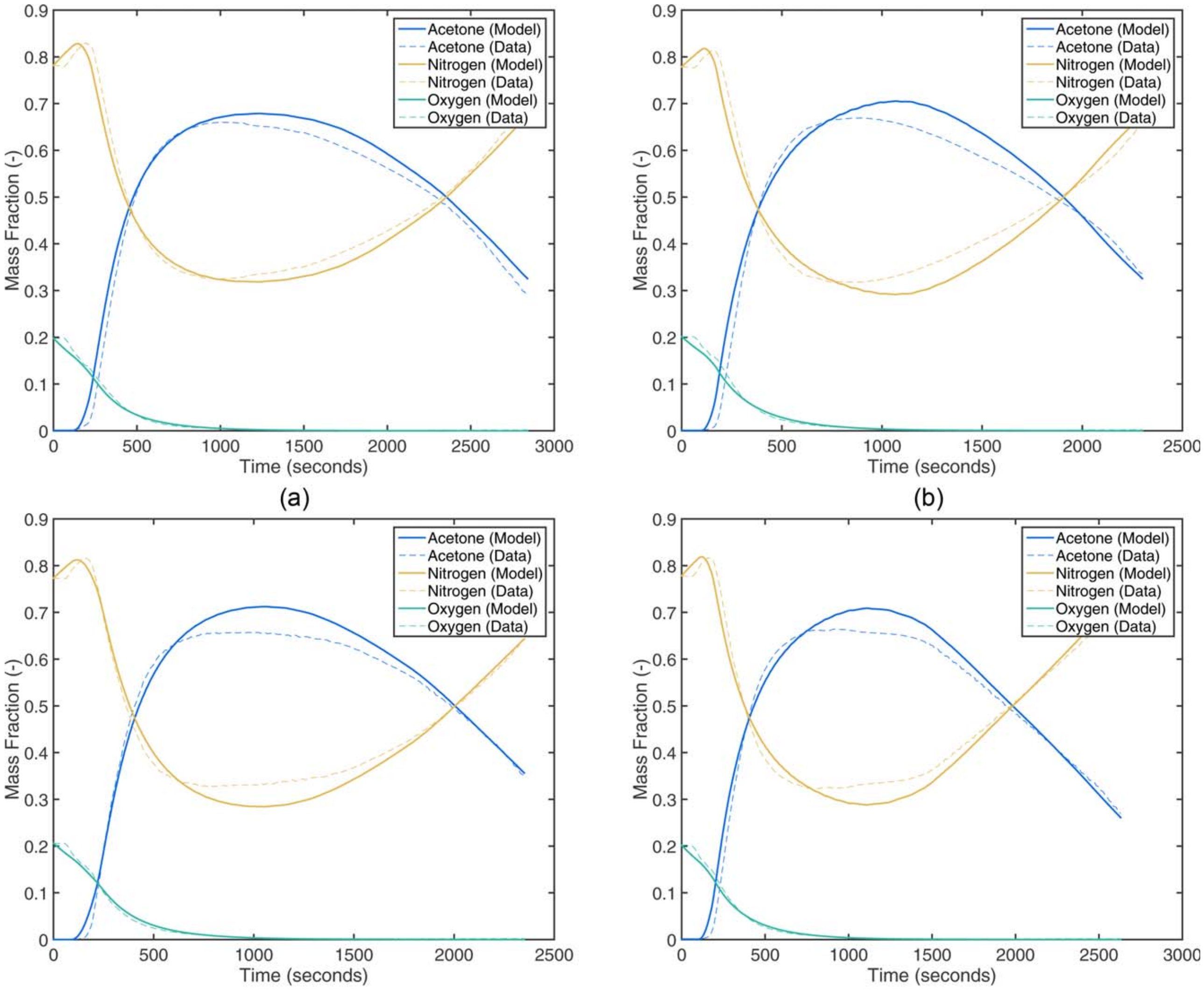

(a) (b)

(c) (d)

Figure 10. Comparison of MS data and oven headspace composition predictions for a particle size range of 150–250 μm.

[Color figure can be viewed in the online issue, which is available at wileyonlinelibrary.com.]

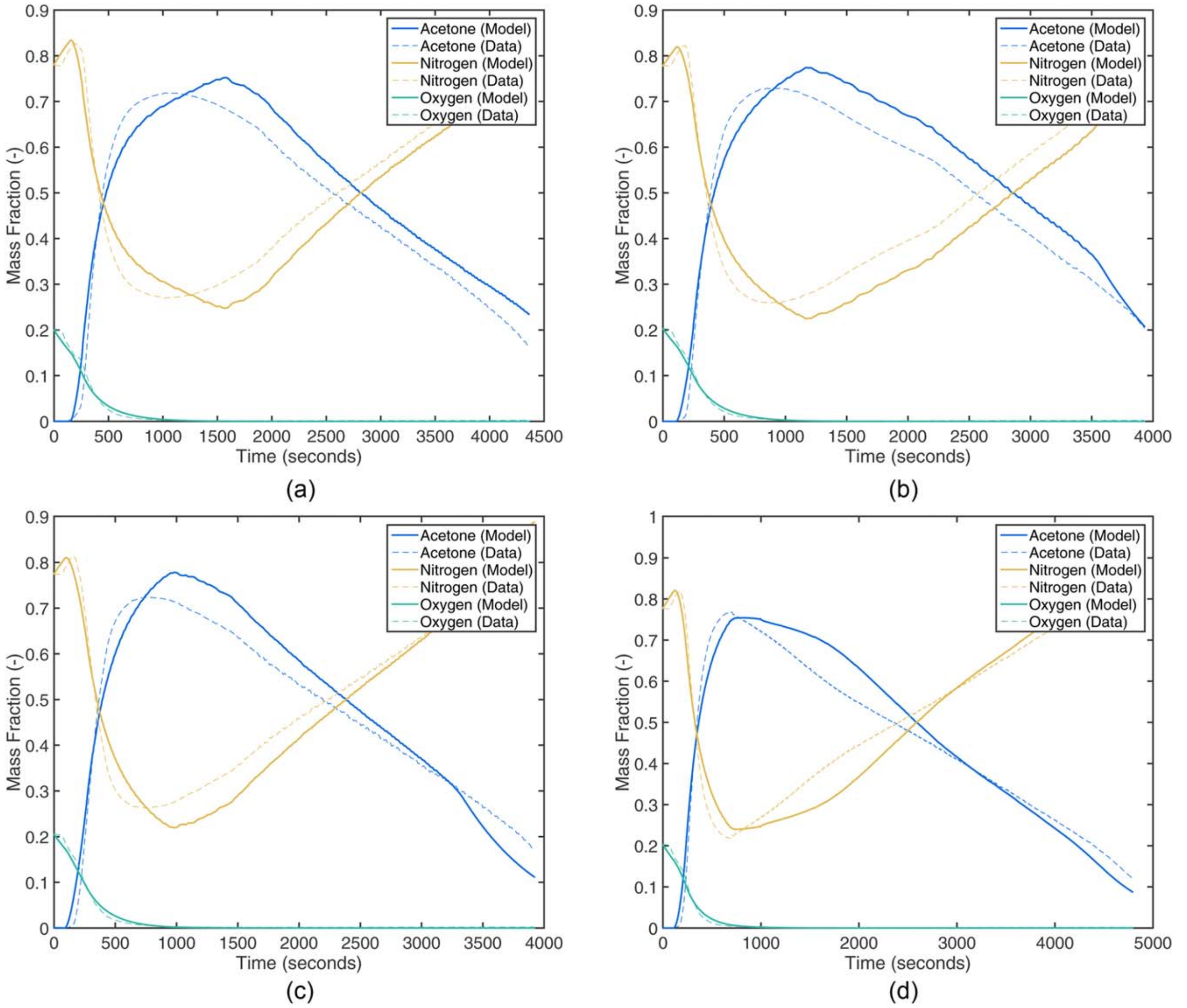

Figure 11. Comparison of MS data and oven headspace composition predictions for a particle size range of 10–25 μm.

[Color figure can be viewed in the online issue, which is available at wileyonlinelibrary.com.]

Table 5. Parameter Estimates Obtained from All Optimization Runs

d_p (μm)	T (°C)	P (torr |× 0.13 kPa)	k_s (W/m K)	h_t (W/m^2 K)	h_{oven} (W/m^2 K)	D_o (m^2/s)	h_{sv-1} (W/m^2 K)	h_b (W/m^2 K)
150–250	40	50	**0.26**	141.47	**55.07**	**8.90 E −06**	**8.95**	**159.98**
70–110	40	50	**0.25**	**141.47**	**98.34**	**6.64 E −06**	**8.43**	**108.45**
10–25	40	50	**0.20**	141.47	**1.24**	**2.62 E −06**	**3.34**	**145.77**
150–250	30	50	0.26	141.47	55.07	8.90 E −06	**1.28**	**175.19**
150–250	50	50	0.26	141.47	55.07	8.90 E −06	**1.72**	**182.57**
150–250	40	40	0.26	141.47	55.07	8.90 E −06	**8.97**	**160.74**
150–250	40	60	0.26	141.47	55.07	8.90 E −06	**4.47**	**189.63**
70–110	30	50	0.25	141.47	98.34	6.64 E −06	**2.99**	**173.16**
70–110	50	50	0.25	141.47	98.34	6.64 E −06	**8.86**	**185.12**
70–110	40	40	0.25	141.47	98.34	6.64 E −06	**2.91**	**178.25**
70–110	40	60	0.25	141.47	98.34	6.64 E −06	**2.56**	**190.44**
10–25	30	50	0.20	141.47	1.24	2.62 E −06	**9.76**	**198.45**
10–25	50	50	0.20	141.47	1.24	2.62 E −06	**5.91**	**193.91**
10–25	40	40	0.20	141.47	1.24	2.62 E −06	**8.79**	**189.72**
10–25	40	60	0.20	141.47	1.24	2.62 E −06	**0.22**	**190.69**

The parameters indicated in a bold font were adjusted for the particular run shown, while the parameters indicated in black were fixed as constants for that run.

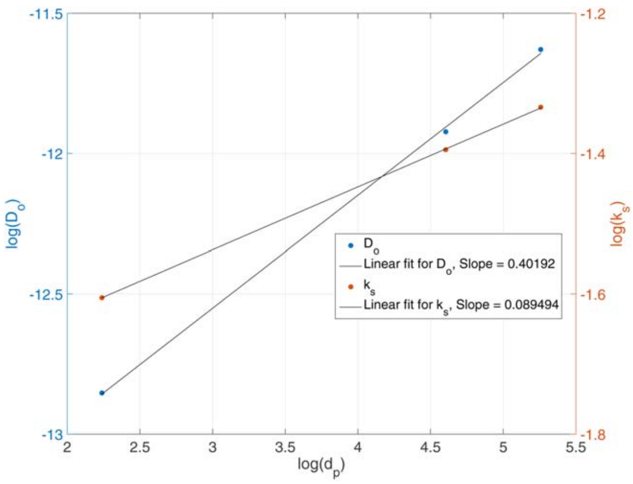

Figure 12. Variation of log(k_s) and log(D_o) with log(d_p), where d_p is the volume weighted mean diameter of the glass beads.

[Color figure can be viewed in the online issue, which is available at wileyonlinelibrary.com.]

acetone at the pressure in the oven. Operating conditions for the experiment were a particle size range of 70–110 μm, a temperature of 40°C, and a pressure of 50 Torr (6.66 kPa). All three temperatures increased during the initial phase, indicated as zone 1 in the figure. We believe that the cake was merely heating during this period with evaporation being negligible, as the MS reading indicated no acetate in the vapor headspace. When the bottom temperature reached T_{sat}, the acetone reading from the MS started to increase rapidly. This point marked the beginning of zone 2, where the acetone at the bottom of the cake began to boil and the bottom temperature began to approximately track T_{sat}. At about 750 s, the bottom temperature exhibited a sharp increase suggesting that all the liquid had been boiled away and the cake was being heated. This point marked the beginning of zone 3, which continued until the end of the experiment. The other two temperatures exhibited similar behavior, with the end of liquid boiling occurring later. This behavior was consistently observed for all experiments in the range of operating conditions considered.

Parameter estimation results

Base Case Conditions. We performed parameter estimation with three different objective functions (χ_{MS}, $\chi_{\mathrm{MS}}+\chi_T$, χ_T) at the base case conditions of 40°C, 50 Torr (6.66 kPa), and 70–110 μm particle size. The six estimated parameter were D_o, k_{s}, $h_{\mathrm{sv-l}}$, h_t, h_{b}, and h_{oven}. In Figure 6, each row corresponds to a different objective function, while the two columns show results for head space compositions and cake temperatures. The quality of prediction was accessed according to the RMS value shown for each case. As would be expected, χ_{MS} produced the most accurate composition predictions, χ_T produced the most accurate temperature predictions, and $\chi_{\mathrm{MS}}+\chi_T$ produced a compromise between the compositions and temperature predictions. Considerable errors were present with all three objective functions, demonstrating the complexity of the vacuum drying process and the value of cake temperature measurements in addition to solvent composition measurements for model development and validation.

Table 4 contains the parameter estimates generated with the three objective functions. Very similar D_o values were obtained, while $h_{\mathrm{sv-l}}$, h_{b}, and h_t agreed with a factor of three or less. Larger differences were observed for k_{s} and h_{oven}, with the h_{oven} value obtained with χ_{MS} much smaller than the other two values. The objective function $\chi_{\mathrm{MS}}+\chi_T$ produced nearly equal values of h_{oven} and h_t. These results were surprising as h_t, which represents the heat-transfer coefficient from the hot fluid through a metal plate to the base layer of particles, would be higher in value than h_{oven}, which represents the heat-transfer coefficient between the top of cake and the oven headspace. The k_{s} value obtained with χ_{MS} was similar to a value (0.15 W/m K) reported in literature for glass beads,[16,19] while the k_{s} values obtained with the other two objective functions were considerably higher. Because the primary goal of this study was to predict the solvent concentration in the cake, all the remaining results used χ_{MS} as the objective function.

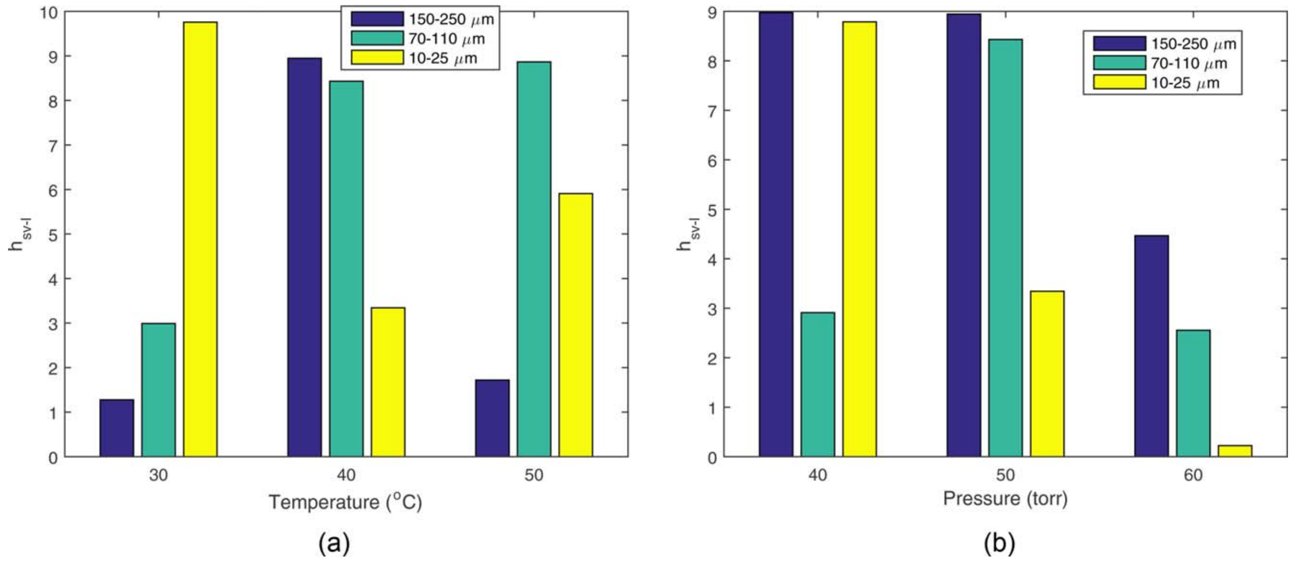

(a)

(b)

Figure 13. Variations in $h_{\mathrm{sv-l}}$ $(\mathrm{W/m^2\,K})$ estimates as a function of temperature and pressure for different particle sizes.

[Color figure can be viewed in the online issue, which is available at wileyonlinelibrary.com.]

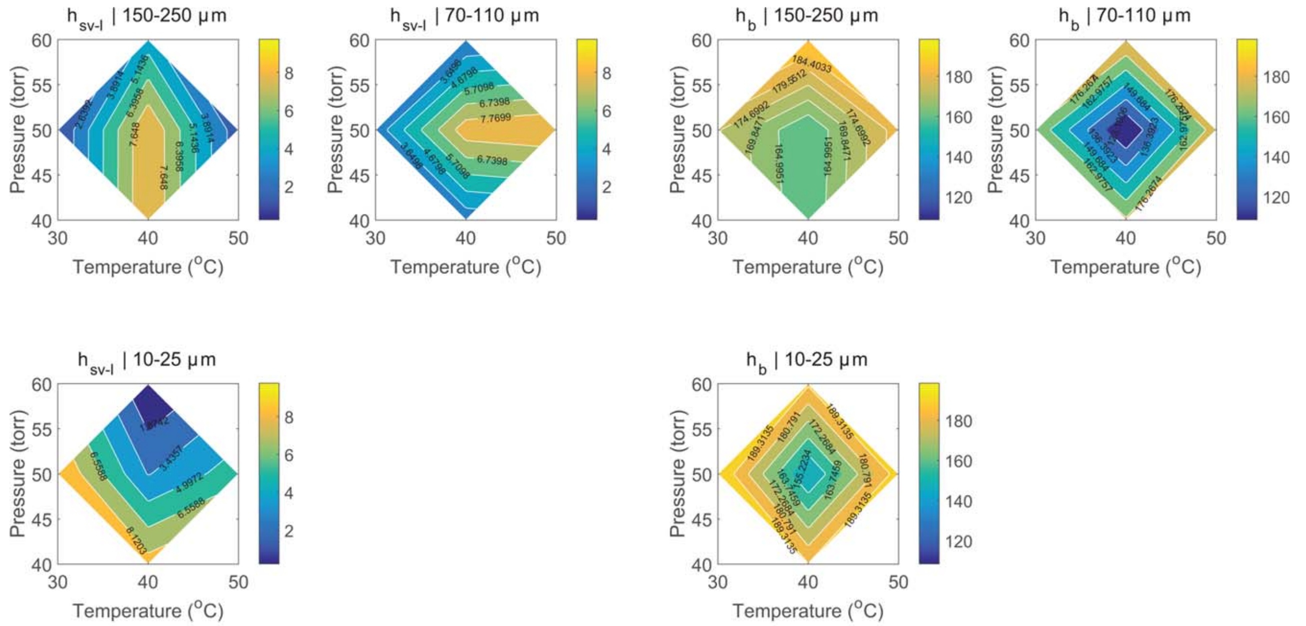

(a)

(b)

Figure 14. Parameter contours for h_{sv-l} $(\mathrm{W/m^2\,K})$ and h_b $(\mathrm{W/m^2\,K})$ as a function of temperature and pressure for different particle sizes.

[Color figure can be viewed in the online issue, which is available at wileyonlinelibrary.com.]

Pressure and Temperature Variations. Next, we performed parameter estimation studies over a range of pressures and temperatures with 70–110 μm glass beads. As explained in the section, Parameter estimation, only the heat-transfer coefficient between the solid-vapor and liquid phases h_{sv-l} and the heat-transfer coefficient between the base layer and the bottom of cake h_b were re-estimated as these two parameters were expected to vary with pressure and temperature. The remaining four adjustable parameters were held constant at their base case values obtained with χ_{MS} (Table 4). Reasonably accurate temperature (Figure 7) and pressure (Figure 8) predictions were generated despite only two parameters being estimated for each case. The reported RMS values demonstrated that the quality of the model predictions were similar to those obtained for the base case conditions. The model matched the temperature data relatively well for the top most layer ($z = 1.8$ cm), but large deviations were observed for the bottom most layer ($z = 0$ cm). We believe that this error was attributable to radial heat transfer from the walls of the dish toward the bottom of the dish, which would cause the material at the bottom-corner of the dish to dry before the material at the bottom-center. This behavior cannot be captured by our 1-D spatial model. Therefore, the exact time when the bottom layer completely dried was difficult to predict. Once dry, the bottom layer increased in temperature quickly causing the adjacent layers to heat more rapidly than predicted. Similar behavior was observed with the pressure variations.

Other Particle Sizes. We performed parameter estimation studies for two other bead sizes (10–25 and 150–250 μm) at the base case temperature (40°C) and pressure [50 Torr (6.66 kPa)] to further analyze the predictive capability of the drying model. Of the six parameters originally used for estimation, only the heat-transfer coefficient between the heating fluid to the base layer h_t was expected to be independent of particle size. Therefore, h_t was fixed at the base case value obtained with χ_{MS} (Table 4) and the remaining five parameters (D_o, k_s, h_{sv-l}, h_t, h_b, h_{oven}) were estimated. The data fits were similar to those generated for the base case condition, with slightly improved fits obtained for the 150–250 μm beads and slightly less accurate fits obtained for the 10–25 μm beads according to the computed RMS values (Figure 9). The same trend was observed with for the cake temperatures.

Temperature and Pressure Variations for Other Particle Sizes. Next, we investigated the ability of the drying model to predict composition data for small and large bead sizes when the temperature and pressure were varied. For each bead size, the parameters k_s, h_t, h_{oven}, and D_o were fixed at the

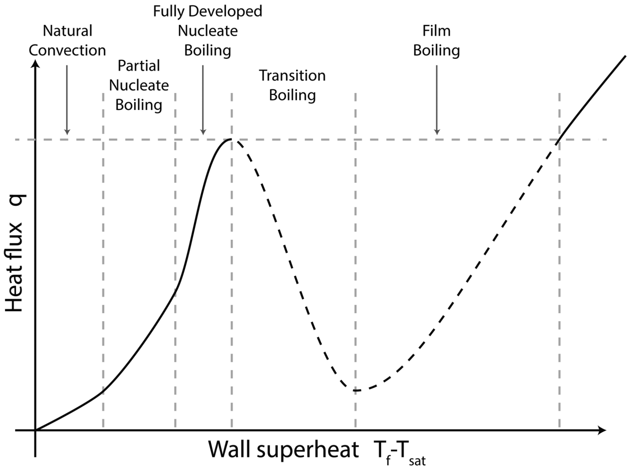

Figure 15. A typical boiling curve showing the variation of the heat flux as a function of the wall superheat. This behavior is also described in Ref. 20.

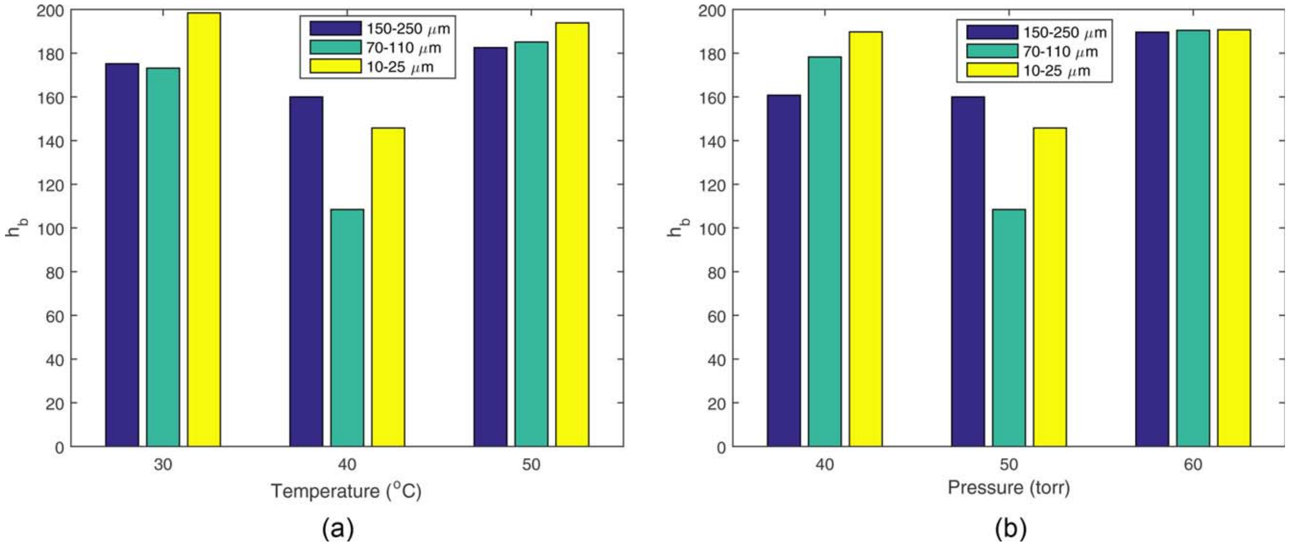

Figure 16. Variations in h_b $(W/m^2 K)$ estimates as a function of temperature and pressure for different particle sizes.

[Color figure can be viewed in the online issue, which is available at wileyonlinelibrary.com.]

values obtained at the base case temperature and pressure (Figure 9) and h_{sv-1} and h_b were re-estimated because only these two parameters were expected to vary for these tests. For the large beads, the model was able to generate composition predictions that were slightly improved compared to the base case conditions (Figure 10). With the exception of low temperature and pressure case, the model also produced slightly improved composition predictions for the small beads (Figure 11).

Analysis of Parameter Estimation Results. The estimated parameters obtained from all the optimization runs are shown in Table 5. The first three rows correspond to glass beads with the particle ranges 150–250, 70–110, and 10–25 μm at the base case conditions of 40°C and 50 Torr (6.66 kPa). The heat-transfer coefficient h_t was obtained from optimization of 70–110 μm beads at base case conditions and then was held constant for all other cases. A different set of the parameters k_s, h_{oven}, and D_o were obtained for each bead size at base case conditions and then was allowed to vary only with particle size. The thermal conductivity of the solid k_s and the diffusion coefficient D_o decreased with decreasing mean particle size. More specifically, $\log(k_s)$ and $\log(D_o)$ appeared to vary linearly with $\log(d_p)$ as shown in Figure 12. The heat-transfer coefficient between the cake and the oven h_{oven} exhibited a peak at 70–110 μm and was two orders of magnitude smaller for the 10–25 μm beads than for the other two bead sizes.

The parameters h_{sv-1} and h_b were allowed to vary with particle size, temperature, and pressure. Figure 13 shows how the estimates of h_{sv-1} varied with particle size at different temperatures and pressures. At 30°C, h_{sv-1} increased with decreasing particle size (Figure 13a). However, the opposite trend was observed at 40°C and no clear trend was evident at 50°C. At 50 and 60 Torr (6.66 and 7.99 kPa), h_{sv-1} decreased with decreasing particle size (Figure 13b). However, no trend was observed at 40 Torr (5.33 kPa). To further analyze the dependence of h_{sv-1} on operating conditions, we prepared plots showing constant h_{sv-1} contours as a function of the temperature and pressure for each bead size (Figure 14a). These plots clearly illustrate that h_{sv-1} exhibited very different dependencies for the three bead sizes.

A possible explanation for the complex dependence of h_{sv-1} on operating conditions is that the heat flux for boiling changes with temperature difference (Ref. 17, p. 767). When plotted as a function of the temperature difference driving force, the heat flux exhibits a local maxima at the beginning of transition boiling and a local minima at the end of transition boiling (Figure 15).

Figure 16 shows how the estimate of h_b varied with particle size at different temperatures and pressures. The estimate exhibited relatively small variations with respect to both temperature and pressure for 150–250 μm beads ($\approxeq 30$ W/m^2 K). Larger variations were observed for the 70–110 μm ($\approxeq 82$ W/m^2 K) and 10–25 μm ($\approxeq 53$ W/m^2 K) beads. Contour plots of h_b vs. temperature and pressure showed no obvious trends with respect to temperature (Figure 15a). While h_b increased with pressure for the 150–250 μm beads, h_b exhibited a minimum for both 70–110 and 10–25 μm beads (Figure 14b). We attributed the lack of clear trends in h_b to the complex phenomenon, which includes the effects of heat transfer from the base layer to the first layer of particles and liquid boiling at the interface, captured by this parameter. Further studies beyond the scope of this article would be needed to better understand these mechanisms.

Conclusions

We constructed a highly controllable vacuum drying system with the capability for measuring both temperatures inside the cake and gas compositions in the oven headspace for the development of multiphase transport drying models. Experiments with glass beads conducted over a range of particle sizes, temperatures, and pressures suggested that boiling (as opposed to evaporation) was the dominant drying mechanism. Once the local cake temperature reached the saturation temperature T_{sat}, the liquid at that location began to boil and the local temperature approximately tracked T_{sat}. Although this phenomenon is evident in another experimental study,[9] we believe that our study provides the first explicit characterization of this boiling behavior.

We developed a MPTM which captured the physics of the drying process more faithfully than existing models under conditions where boiling was the predominant mode of solvent loss. The model was based on several simplifying assumptions, including that evaporation was negligible and that the vapor and solid phases could be lumped into a single phase. To investigate the predictive capabilities of the model, parameter estimation studies were performed using a dataset consisting of headspace composition measurements collected for three bead sizes (10, 100, 200 micron volume averaged means), three temperatures (30, 40, 50°C), and three pressures (40, 50, 60 Torr or 5.33, 6.66, 7.99 kPa). The parameters estimated consisted of the liquid diffusion coefficient, the thermal conductivity of the solid and four heat-transfer coefficients. First, we established a base set of parameter estimates at one operating condition. Then, according to the assumptions mentioned in the Parameter Estimation section, certain parameters were re-estimated as the bead size, temperature of pressure were varied.

We found that the parameterized model was capable of producing composition time profile estimates with 2.5–4% error according to calculated RMS values. Conversely, temperature measurements within the cake could only be reproduced in a qualitative manner, suggesting that the model lacked some process physics. The thermal conductivity and the diffusion coefficient were shown to have a linear dependence on mean particle size when variable were expressed in logarithmic coordinates. Other parameter trends with particle size were difficult to discern and we contribute this to the complex nature of boiling (Ref. 17, p. 767). Natural extensions of our model include the development of a full three phase description and the incorporation of evaporative drying mechanisms.

Acknowledgments

The authors wish to acknowledge Sunovion Pharmaceuticals for funding this research and for providing facilities to perform the drying experiments. The authors thank the following individuals for their assistance: John Barck (Sunovion) for custom building the vacuum oven and for other miscellaneous improvements to the laboratory-scale drying system; Bob Prytko, Vitaly Nivorozhkin, Robert Bujalski, and Mike Filios (Sunovion) for constructing, operating, and maintaining the drying system; Mike Sizensky (Sunovion) for performing particle-size distribution measurements of the glass beads; and Mike Eck and Charles DeCarlo (Extrel) for supporting our use of the MS.

Notation

Inputs

α = surface area to volume ratio of the beads, m^{-1}
β = fraction of solid surface area in contact with liquid
ΔH = enthalpy of vaporization, J/kg
$\dot{\Gamma}$ = rate of vaporization of liquid per unit volume, kg/m^3 s
$\dot{m}_{out}$ = mass flow rate out of the oven headspace, kg/s
$\dot{m}_{purge}$ = mass flow rate of purge gas into the oven headspace, kg/s
$\dot{m}_{sol}$ = mass flow rate of solvent vapor into the oven headspace, kg/s
ϵ_i = volume fraction of "*i*"
ϵ_{void} = void volume fraction of the cake
ρ_i = density of "*i*," kg/m^3
A_c = cross-section area of cake, m^2
C_i = concentration of "*i*," kg/m^3
c_{p_i} = heat capacity of "*i*," J/kg K
$c_{p_{avg}}$ = specific heat capacity of gas in oven headspace, J/kg K
$c_{p_{purge}}$ = specific heat capacity of purge gas entering the oven headspace, J/kg K
D = diffusion coefficient of liquid, m^2/s
h = enthalpy of gas in oven headspace, J/kg
h_l = heat capacity of liquid at T_l, J/kg
h_v = heat capacity of vapor at T_l, J/kg
h_{out} = enthalpy of purge gas entering the oven headspace, J/kg
h_{purge} = enthalpy of vaporization, J/kg
h_{sol} = enthalpy of solvent vapor entering the oven headspace, J/kg
k_i = thermal conductivity of "*i*," W/m K
L = thickness of the cake, m
m = mass of gas in oven headspace, kg
m_l = initial mass of liquid in cake, kg
m_s = mass of solid in cake, kg
t = time, s
T_f = temperature of the heating fluid, K
V_c = volume of the cake, m^3
z = distance from bottom of cake, m

Parameters

D_o = diffusion coefficient of liquid when the cake is saturated, m^2/s
h_b = heat-transfer coefficient between base layer and bottom of cake, W/m^2 K
h_t = heat-transfer coefficient between heating fluid and base layer, W/m^2 K
h_{oven} = heat-transfer coefficient between the top of cake and the oven headspace, W/m^2 K
h_{sv-l} = heat-transfer coefficient between solid-vapor and liquid phase, W/m^2 K
k_s = thermal conductivity of solid, W/m K

Subscripts

b = base layer
l = liquid
s = solid
sv = solid-vapor phase
v = vapor

Variables

ϵ_l = volume fraction of liquid
T_b = temperature of the base layer, K
T_l = temperature of liquid phase, K
T_{oven} = temperature of oven headspace, K
T_{sv} = temperature of solid-vapor phase, K
x_i = mass fraction of species "*i*" in oven headspace

Literature Cited

1. Murru M, Giorgio G, Montomoli S, Ricard F, Stepanek F. Model-based scale-up of vacuum contact drying of pharmaceutical compounds. *Chem Eng Sci.* 2011;66(21):5045–5054.
2. Sahni EK, Chaudhuri B. Contact drying: a review of experimental and mechanistic modeling approaches. *Int J Pharm.* 2012;434(1): 334–348.
3. Whitaker S. Simultaneous heat, mass, and momentum transfer in porous media: a theory of drying. *Adv Heat Transf.* 1977;13:119–203.
4. Kohout M, Stepanek F. Multi-scale analysis of vacuum contact drying. *Dry Technol.* 2007;25(7–8):1265–1273.
5. Sandoval-Torres S, Rodríguez-Ramírez J, Méndez-Lagunas L. Modeling plain vacuum drying by considering a dynamic capillary pressure. *Chem Biochem Eng Q.* 2011;25(3):327–334.
6. Nadi F, Rahimi G, Younsi R, Tavakoli T, Hamidi-Esfahani Z. Numerical simulation of vacuum drying by Luikov's equations. *Dry Technol.* 2012;30(2):197–206.
7. Perré P, Turner IW. A 3-D version of TransPore: a comprehensive heat and mass transfer computational model for simulating the drying of porous media. *Int J Heat Mass Transf.* 1999;42(24):4501–4521.
8. Su SL. Modeling of multi-phase moisture transfer and induced stress in drying clay bricks. *Appl Clay Sci.* 1997;12(3):189–207.

9. Laurent S, Allouche J, Couture F, Roques M. Thermal behaviour of a multicomponent solvent pharmaceutical hydrate during vacuum contact drying. *Int J Therm Sci.* 1999;38(8):695–702.
10. Wolfram Alpha LLC. 2014. Wolfram|Alpha. https://www.wolframalpha.com/input/?i=boiling+point+of+acetone+at+50+torr (access October 17, 2014).
11. Dodda AG, Saranteas K, Henson MA. Using online mass spectrometry to predict the end point during drying of pharmaceutical products. *Org Process Res Dev.* 2015;19(1):122–131.
12. Guideline IHT. Impurities: guideline for residual solvents Q3C (R3). *Curr Step.* 2005;4:7–8.
13. Kom PK, Cook W, Kougoulos E. Impact of laboratory vacuum contact drying on material drying rates and physical properties. *Org Process Res Dev.* 2011;15(2):360–366.
14. Sakatani N, Ogawa K, Iijima Y, Honda R, Tanaka S. Thermal conductivity of glass beads as a model material of regolith. *43rd Lunar and Planetary Institute Science Conference Abstracts*, Vol. 43, The Woodlands, Texas, 2012.
15. Presley MA, Christensen PR. Thermal conductivity measurements of particulate materials 1. A review. *J Geophys Res: Planets.* 1997; 102(E3):6535–6549.
16. Presley MA, Christensen PR. Thermal conductivity measurements of particulate materials 2. Results. *J Geophys Res: Planets.* 1997; 102(E3):6551–6566.
17. Faghri A, Zhang Y. *Transport Phenomena in Multiphase Systems.* Burlington, MA 01803, USA: Academic Press, 2006.
18. Welty JR, Wicks CE, Rorrer G, Wilson RE. *Fundamentals of Momentum, Heat, and Mass Transfer*, 4th ed. New Delhi, Delhi 110002, India: Wiley, 2009.
19. Huetter ES, Koemle NI, Kargl G, Kaufmann E. Determination of the effective thermal conductivity of granular materials under varying pressure conditions. *J Geophys Res: Planets.* 2008;113(E12):5–6.
20. Patankar NA. Supernucleating surfaces for nucleate boiling and dropwise condensation heat transfer. *Soft Matter.* 2010;6(8):1613–1620.

Manuscript received Feb. 27, 2015, and revision received May 9, 2015.